# Reduced Dimensionality in Drift-Diffusion Models of Back-Contact Solar Cells and Scanning Photocurrent Microscopy

Robin D. Lamboll and Neil C. Greenham
*Cavendish Laboratory, University of Cambridge,*
*JJ Thomson Avenue, CB3 0HE Cambridge, UK*
(Dated: August 30, 2017)

Solar cells are three-dimensional objects frequently modeled as being one-dimensional for convenience. However, for more complex designs of solar cell or if the cell is only illuminated at one point, one-dimensional modeling is insufficient. Here, some conditions for reducing the complexity of multidimensional drift-diffusion simulations are investigated in realistic situations for a back-contact perovskite solar cell. The analysis investigates under what situations we may neglect vertical carrier density variation and approximate extraction currents to be linearly dependent on the vertically averaged carrier concentration. Analytic expressions for the linear relationship in both the low and high extraction velocity regimes are demonstrated, and the conditions where these approximations break down are investigated. It is shown that recombination is usually accurately modeled using only vertically averaged carrier concentrations when the distance between electrodes is many times the height and when less than half the charges that are generated recombine, although edge effects around the onset of electrodes are noted. These findings are then applied to a problem that often emerges in scanning photocurrent microscopy, a point-excited film with a laterally offset electrode. It is demonstrated that we expect the current recorded in this case to decay exponentially with the distance between excitation and electrode, with a decay constant that can be related to device parameters. The characteristic equilibration time for the system to reach this current, which can be extracted from the phase delay in a lock-in amplifier measurement, is demonstrated to increase linearly with distance. It is shown that information about the diffusion and recombination rates can be extracted from a wide variety of planar systems.

## I. INTRODUCTION

In thin-film solar cells, one type of carrier is typically extracted from the front surface through a transparent conducting electrode and the other through the back layer, via a reflective metal electrode. However, as transparent materials are always limited in conductivity, other cell designs are also used. One group of designs features both types of electrodes on the back side of the device: back contact solar cells [1]. The front of the solar cell can then be freely designed for optimum optical properties and the rear for electrical properties [2], [3]. Alternatively, the front transparent conductive layer can be replaced with a grid of opaque metal – provided the diffusion length of charges in the material is large and hence the grid can be coarse, the area overshadowed by the electrodes need not be large, and conduction to the high-conductivity grid can happen through the bulk [4], [5]. However these designs significantly complicate the modeling of carrier motion in cell operation; for unpatterned cells, a simple one-dimensional model of behavior perpendicular to the plane of the cell is sufficient, but with electrodes placed in patterns, lateral carrier motion must also be investigated. Typically the problems are appropriate for drift-diffusion modeling, a semi-classical macroscopic transport model based on the continuity equations and Poisson's equation [6]. Drift-diffusion models in two and sometimes three dimensions [7–11] are well-known in papers devoted to modeling, but for computational ease or to give analytical solutions, it is generally preferred that the simulation be set up to require as few dimensions as possible. In this report, we will investigate conditions for reducing the dimensionality of the models. We will use device parameters in keeping with dopant-free methylammonium halide perovskite performance for example purposes. Perovskites were chosen as an example system of great interest due to achieving high power conversion efficiencies in a short space of time [12], however we do not attempt to model the specifics of these devices here.

We will first investigate uniform illumination, in which case the model is approximately two-dimensional, and find the conditions under which we may model this in one, lateral dimension. Having established this, we will then investigate how this applies to a scanning photocurrent microscope setup (also known as optical beam-induced current, or OBIC). In this sys-

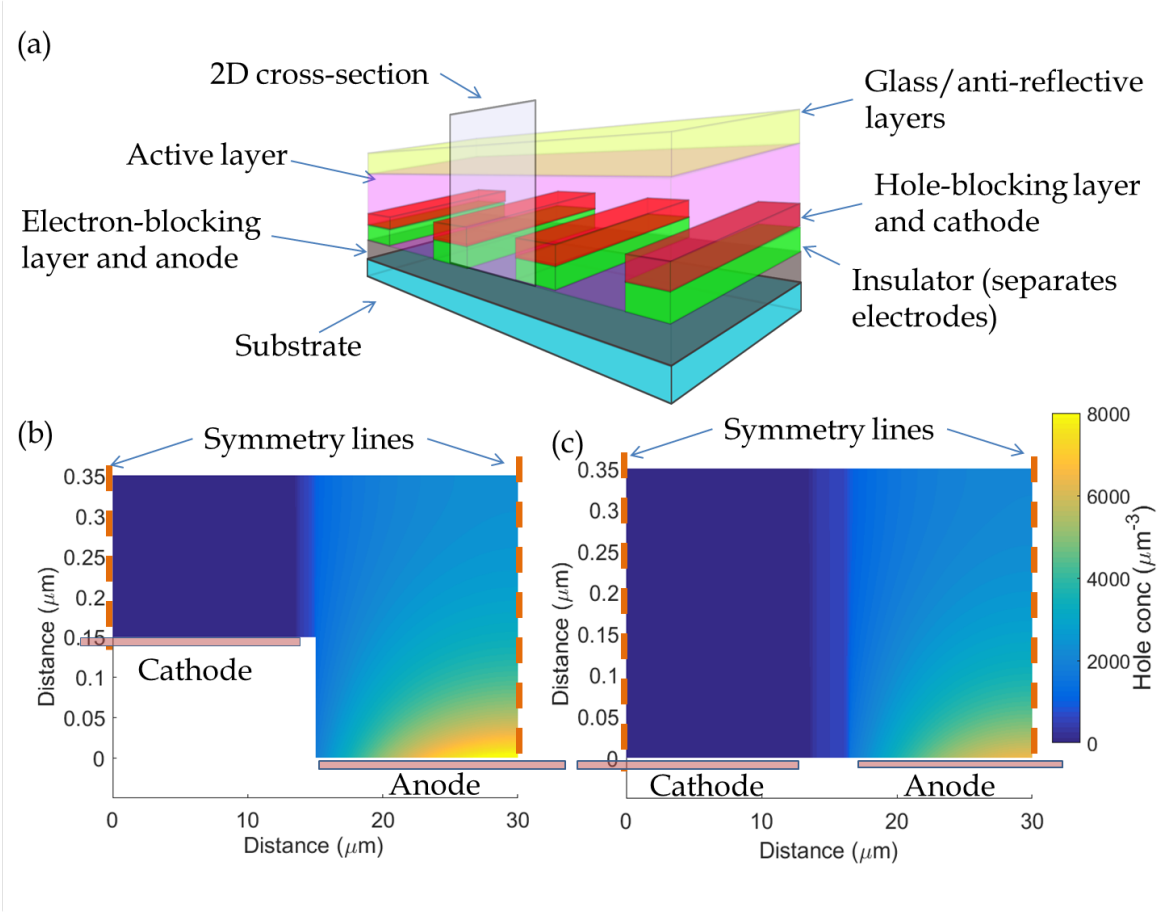


Figure 1. Reducing back-contact solar cells to two dimensional objects. The lower images are different geometries for two-dimensional cross-sections of three-dimensional structures like (a), with (b) simply projected, leaving a step-shaped active layer, and (c) an alternative design with the anode/electron-blocking layer level with the cathode/hole-blocking layer. The symmetry lines represent the midpoints of the electrodes, about which there is reflective symmetry. Simulations conducted using the default parameters explained in the supplementary materials, designed to be realistic for perovskite systems.

tem, a small laser spot excites a region of semiconductor and the current that reaches electrodes is monitored [13]. Here we see lateral transport of carriers under point illumination, but the symmetry-breaking effect of the localized illumination means the full solution is three-dimensional. We will show that in many experimental cases, this will give rise to a current that decays exponentially with distance from the patterned electrodes, and that this current is reached with a characteristic time-delay linear in distance.

Point illumination experiments on planar systems are used to investigate carrier dynamics in the active layer of solar cells or transistors, for instance carrier diffusion and recombination, in a wide variety of materials and systems [14–20]. There are also experimentally different setups that give rise to mathematically similar problems, such as electron beam-induced current measurements of solar cells [21]. These techniques are often used to study nanowires, where the analysis needs only one dimension [13]. In the planar systems considered here, the problem to be solved is more complex, yet in experimental papers on three-dimensional materials such as these, only one-dimensional, simplified versions of the drift-diffusion equations are solved. As shown numerically for a two-dimensional system by [13], we may extract the diffusion length

from this measurement as being the characteristic length of an exponential decay. This is in keeping with the monoexponential decays often encountered experimentally [14, 19, 20], however the conditions under which the approximation holds have not been investigated. Here, we will demonstrate the similarity of numerical and analytic solutions and therefore the applicability of the analytic solutions to a range of problems. We will also investigate what physical parameters can be extracted from these analytic solutions in different cases. We will further show that the delay between signal and measurement gives another avenue to investigate carrier behaviour and explain how these measurements can be combined.

## II. INVESTIGATING THE APPROPRIATENESS OF ONE-DIMENSIONAL MODELS FOR LATERAL DIFFUSION

For many back-contact electrode systems, the electrodes are hundreds of microns in one lateral dimension but only microns in the other, and around a tenth of a micron in height. Under uniform illumination, there will be no variation over the largest dimension, except near the edges of the cell. We can therefore model only the cross-section of the device, as shown in Figure 1a. However the smaller dimensions must be treated more carefully, so we will set up a two-dimensional model and investigate when it can be contracted to one, lateral dimension.

The two-dimensional drift-diffusion simulations are loosely based on perovskite quasi-interdigitated solar cell structures as found in [22], with formulae used and device parameters listed in the supplementary materials. The geometry of the structure is either step-shaped, with one electrode raised, as in [22] and Figure 1b, or flat, with both electrodes level on the bottom, as in Figure 1c. In the step case, the anode runs along the entirety of the base but the cathode only runs along 90% of the raised step, to present a 'lip' of the insulator. The cathode is raised by 150 nm, out of a total height of 350 nm. The flat structure has electrodes along 90% of each half and an insulating patch in-between. The horizontal edges of the simulation are the middles of the electrodes - with uniform illumination, these will be symmetry lines of the system. At the insulating boundaries and the symmetry lines, zero perpendicular electric field and zero electron/hole current conditions are imposed. Within the active area, carriers are generated a rate that exponentially decays from the surface. They travel and recombine according to the steady state drift-diffusion equations as described in the supplementary materials. Under the conditions used, recombination will primarily be Shockley-Read-Hall (SRH). The simulations do not include ions or dopants, and are performed with no effective applied field.

We assume that in two or three dimensions, the current flux into an electrode is proportional to the local concentration of one carrier type at the interface: $J = qv_s n_{interface}$, for $q$ the carrier charge. It is assumed that blocking layers mean that each electrode selectively accepts only one carrier type. If surface recombination is included, it may be considered in the same way, with a smaller $v_s$ for the majority carrier type. This physical extraction velocity $v_s$ may tend to infinity and zero in the Ohmic and blocking cases respectively.

To vertically contract this and make a 1D system, the relationship between the electron or hole current into the electrode and the average carrier density above should be simple; to avoid detailed modeling, it should preferably be linear. Since with no carriers we have no current, the linear trend has zero offset:

$$J = qv_{1D}\overline{n}, \tag{1}$$

for $\overline{n}$ the vertically averaged carrier density and $v_{1D}$ the effective extraction velocity. We therefore run the simulation with many values of $v_s$ and plot the dependence of current extracted against the vertically averaged carrier concentration at that $x$-position for each simulation, and search for a linear trend.

Figure 2a shows the relationship between the current density flowing into a short stretch of an electrode and the vertically averaged electron concentration above it, for data taken from anodes below a step. We see that in systems with wider electrodes this zero-offset linear trend from equation 1 is usually shown to be a good assumption, although non-linearity is visible at either ends of the trend.

At the low-concentration end, this is due to a population of carriers held away from the electrodes. This arises due to attraction between the carriers, one type of which is blocked from the electrode below. The high concentrations

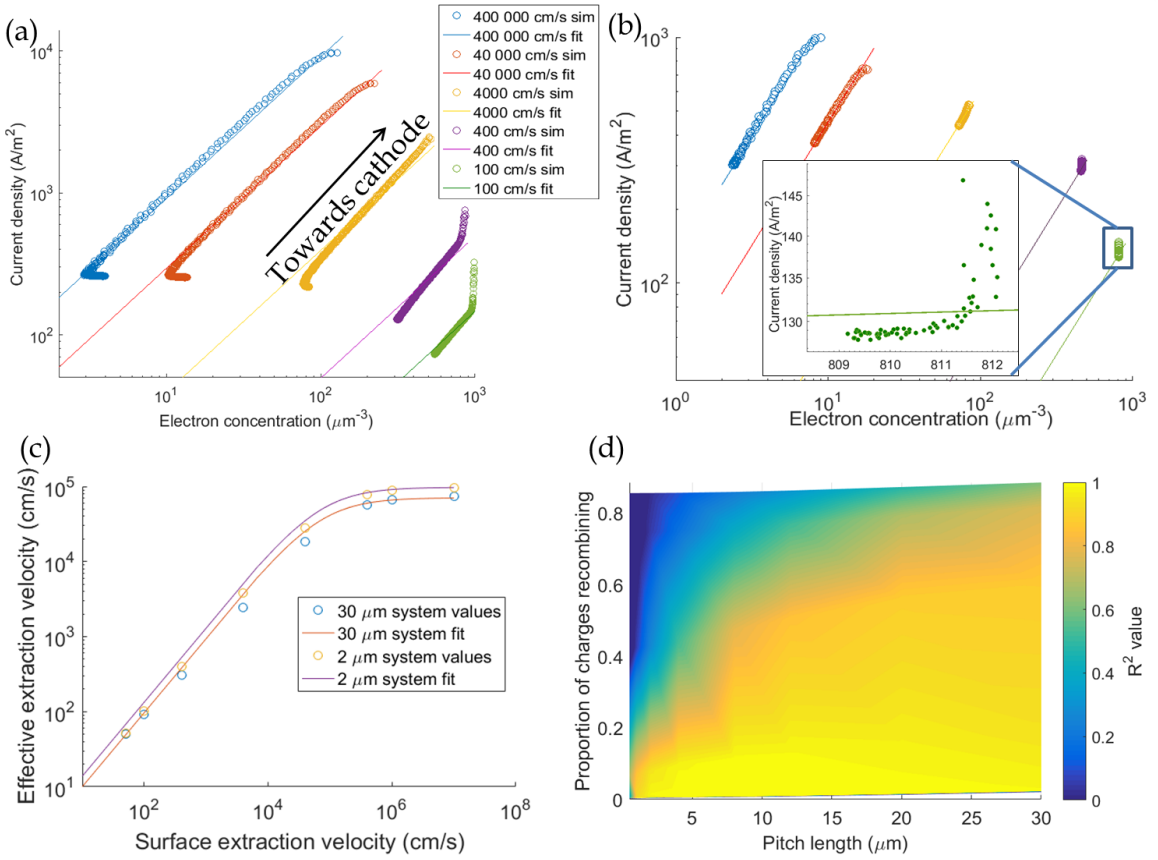


Figure 2. (a, b): Relationship between current extracted and vertically averaged electron concentration for a variety of extraction velocities, for the lower electrode for (a) 30 µm simulation pitch length, (b) a 2 $\mu$m pitch length. Inset magnifies the distribution in the 100 cm/s simulation. (c): relationship between extraction velocity at the electrode and effective one-dimensionally averaged extraction velocity (e.g. gradient of lines in (a)) for flat electrodes of different lengths. (d): Coefficient of determination, $R^2$, for the linear fits to density-concentration data as in (a) and (b). (All images): Both carrier types have a diffusion constant of 1.5 cm$^2$/s and distributions are from a step-electrode system, as in Figure 1b.

of blocked carriers give rise to voltage maxima above the centerpoints of the electrodes (image in supplementary materials) that keep the accepted carriers away from the electrode. This effect is therefore not seen in Figure 2b, where the lengthscale and carrier concentrations are too small for the total voltage difference over the system to be large compared to the thermal voltage, $V_T = k_B T/e$. It is also not seen if the simulation is run with the effects of the electric field switched off (see supplementary materials). At the high concentration end, there are slightly different irregularities due to factors affecting diffusion and recombination.

In the high extraction velocity limit, there is a slight decrease in current extracted below the step of the electrode, as many of the electrons are initially generated above the step and therefore have slightly further to travel to reach the electrode compared to those generated above it. However, when charge extraction is slower, recombination is more important and the precise location of generation less important. In the low extraction velocity limit we see a strong increase in current from a small increase in concentration, arising near the step. This is because there are fewer holes here, and therefore proportionally less recombination. With much smaller systems, there is little variation in either the collected current or the vertically averaged carrier density, as

seen in Figure 2b. This is because the lateral diffusion and vertical diffusion are comparable to each other and to the carrier diffusion length, allowing homogenisation.

The trend lines of graphs like these give us the value of the effective extraction velocity, $v_{1D}$, from equation 1. Figure 2c shows how this varies with the actual extraction velocity. We see that in the slow-extraction limit, the effective extraction velocity equals the extraction velocity at the electrode. This is because the carrier concentration becomes fairly uniform, so $n_{interface} \approx \overline{n}$ and $v_{1D} \approx v_s$. In the high extraction velocity limit, the concentration at the electrode tends to 0 and the effective velocity tends to a diffusion-dominated value.

However we also need to consider the accuracy of the fit itself. To explore this systematically, we investigate what proportion of the variance of the data can be ascribed to the linear fit and what proportion needs a more complicated model. The $R^2$ value of a fit measures what fraction of the variability that fit explains. We see in Figure 2d that systems smaller than about 0.35 $\mu$m (the system height) have a poorer fit and a lower $R^2$ value, as do those with a lower extraction speed. The physical explanation for the latter is that it increases the impact of recombination on the system. Recombination competes with charge extraction in non-trivial ways, as it depends on the concentration of countercharges. We find that $R^2$ values are always greater than 0.95 for systems with more than half of the charge extracted, provided the system is at least three times wider than it is high. However, as shown in the supplementary materials, if we are concerned with the proportional error in the fit rather than the $R^2$ value and explanatory power of the model, problems also emerge for long systems - in this case, large relative errors occur with a pitch length over 15 $\mu$m. This is mainly because in larger systems there are more charges near the edge of the electrodes, magnifying the effects of any non-linearity.

The form of the effective extraction velocity can also be estimated. We require the current at the interface to equal the effective current out from the bulk: $j_n = v_{1D}\bar{n} = v_s n_s$. The carriers arrive at the interface largely by diffusion, and we can approximate this as $j_n = (\bar{n} - n_s)v_d$ for some diffusion speed $v_d$. Equating these and eliminating the carrier concentrations, we find the effective velocity is the harmonic mean of the extraction velocity and the diffusion speed:

$$v_{1D} = \frac{v_s v_d}{v_s + v_d}. \tag{2}$$

We see in Figure 2c that equation 2 fits well, with $R^2$ values consistently above 0.99 if $v_d$ is fitted to the system. We expect the value of this diffusion speed to change upon changing the diffusion constant, so to investigate this we plot the behaviour of the system when one carrier (holes in this case) has its diffusion constant changed. Results are plotted in Figure 3a, for high extraction velocity ($v_s$=1000 000 cm/s), where we expect $v_{1D} = v_s$. Figure 3b then plots the effective velocity as a function of diffusion constant for many such experiments with different electrode lengths. We see the relationship is fairly linear at first, although falls off, particularly for larger systems.

This trend may be compared with one-dimensional expectations. In the low extraction velocity regime, we expect the relationship $v_{1D} = v_s$, and can see the relationship holds well in Figure 2c for $v_s \ll v_d$. In the high extraction velocity regime, with no recombination, no electric fields and with a simple exponential Lambert-Beer law generation function, we expect $D\nabla^2 n = -A\exp(\alpha z)$, for $\alpha$ the absorption constant, $A$ the density of photons absorbed at the bottom of the device and $z$ the vertical height, with maximum $h$. We have the boundary conditions $n(0) = 0$, due to fast recombination at the interface, and $\partial n/\partial x\,(h) = 0$ since there is no extraction at the surface. This has solution

$$\begin{aligned} n(z) &= \frac{A}{D\alpha}\left(\frac{1-\exp(\alpha z)}{\alpha} + z\exp(\alpha h)\right) \\ \Rightarrow v_d &= \frac{D\nabla n|_{x=0}}{\overline{n}} = \frac{D\left(\exp(\alpha h)-1\right)h}{\frac{h}{\alpha} - \frac{e^{\alpha h}}{\alpha^2} + \frac{1}{\alpha^2} + \frac{h^2}{2}e^{\alpha h}}. \end{aligned} \tag{3}$$

This has a limit of $3D/h$ as $\alpha \to 0$ (i.e. under vertically uniform illumination), and is $2.3D/h$ for the values in our simulation.

As can be seen in Figure 3b, at high extraction speeds and low diffusion constants this matches with detailed, two-dimensional simulations including electric fields and recombination, particularly for smaller systems, but begins to break down in larger systems when electron and hole diffusion constants are very different. More details of this breakdown can be seen in the supplementary materials. For wider systems (i.e. width

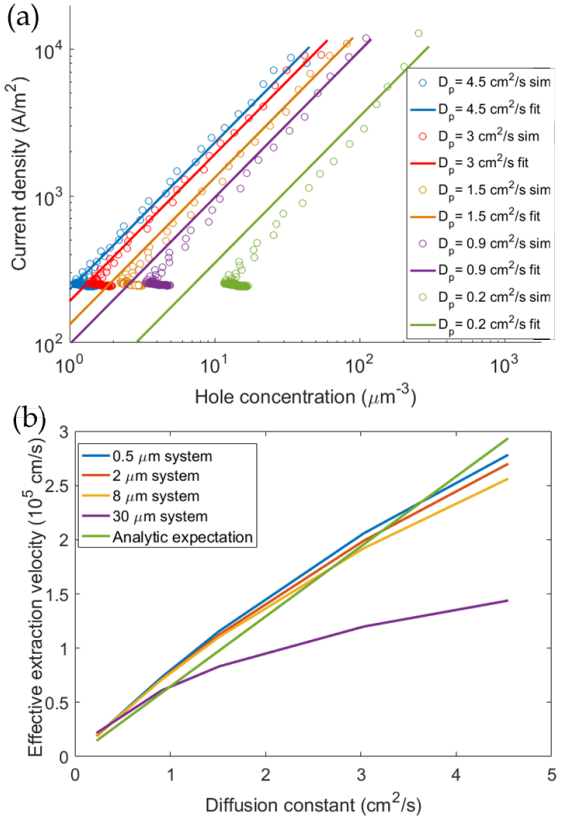


Figure 3. (a): The relationship between mean hole concentration and hole current density when the diffusion constant of the holes is varied but that of electrons left constant at 1.5 cm$^2$/s, for a 30 $\mu$m system. There are no other differences between electrons and holes in this system. Data from simulations in flat systems with a surface extraction velocity of 10 000 cm/s. (b): how the effective velocity depends on the diffusion constant in simulations of different lateral width. Simulations as in (a).

approaching 100 times the height), the carrier buildup is substantial, resulting in electrostatic potentials that are comparable to the thermal voltage. There are also higher levels of recombination so we expect to see the failure of equation 3. However for systems narrower than this but wider than the system height, the analytic expressions obtained by combining equations (2) and (3) provide a good description of the system.

In order to one-dimensionalise the system, we also need to be able to calculate the actual recombination from the vertically averaged $n$ and $p$ values. In the limit of one carrier type being very scarce (say, $n$), the SRH recombination equation reduces to $R = n/\tau_1$, in which case using the vertically averaged value of $n$ will work exactly. The situation is nontrivial if both species are common enough that there is a significant component of bimolecular recombination, or if both species have similar concentrations, so that the SRH recombination is limited by both species. In these cases, the applicability of the one-dimensionalised model depends on how the density of carriers changes thoughout the film.

Figure 4a shows the relationship between electron concentration and recombination when vertically averaged over the anode of a flat system, in the limit of fast charge extraction. We see that in systems with wide pitch distances, recombination matches the simple limit, $n/\tau_1$. This is not the case in smaller systems, where there is clear deviation from this line, which is due to both carrier types having similar concentrations. This means we cannot prove that averaged values of carrier concentrations will give us the correct amount of recombination. However, in Figure 4b we compare the actual averaged recombination with the recombination calculated from averaged values, including data from across the device. We see that the recombination is satisfactorily described by the full, one-dimensionalised relationship for all electrode widths. This is because bimolecular recombination is minor in all cases, and the absolute variation in carrier concentration over the height of the cell is small for the minority carrier.

In the limit of slow charge extraction, charge accumulates and bimolecular recombination becomes relevant. Figure 4c shows that the monomolecular-only model fails to describe the system. In this case, the accuracy of the one-dimensionalisation is highly conditional on the precise nature of carrier distributions, however we see in Figure 4d that it is still typically very accurate, if less accurate than the case with only monomolecular recombination in Figure 4b. This is because in this limit, we see very little variation in carrier concentration with height. If bimolecular recombination is dominant at low particle concentrations, modeling it may be more problematic.

For situations like ours, recombination may therefore be easily and accurately modelled using only averaged $n$ and $p$ values. Generation is not dependent on carrier concentration, so while it may need a two-dimensional calculation to establish what value should be used, it is not problematic to use a one-dimensional value for it in calculations. This means that if the

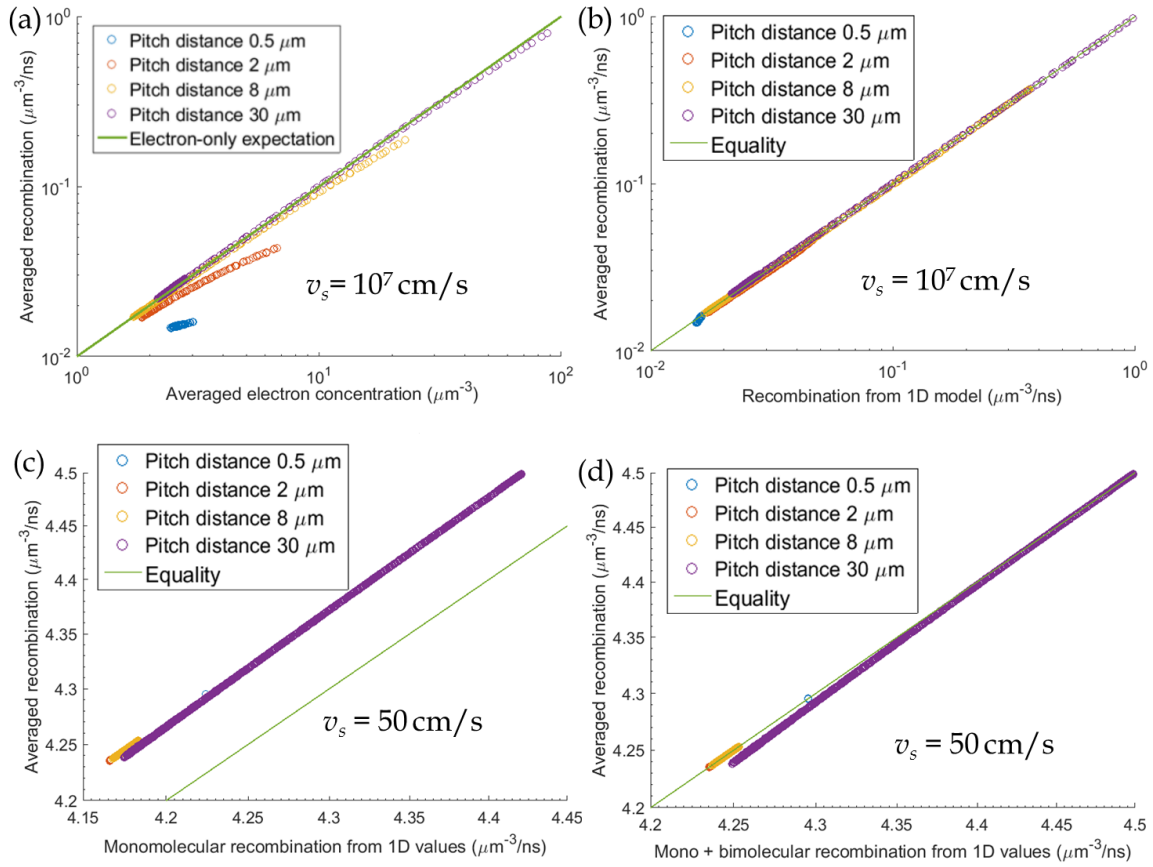


Figure 4. (a): Relationship between the vertically averaged minority carrier (electron) concentration and the vertically average recombination in a flat system with extraction velocity 10 000 000 cm/s at both electrodes and no surface recombination. The data is taken over the electron-accepting anode. This is compared to the simplest, electron-only model. (b): Relationship between the one-dimensional monomolecular recombination that would be expected, given both the vertically averaged electron and hole concentrations, and the total recombination calculated in the full two-dimensional model. Data taken from the same simulations as in (a), but across the whole simulation. (c,d): The same as (b), but with extraction velocity 50 cm/s at both electrodes. (d) includes both monomolecular and bimolecular terms in the one-dimensional recombination calculation.

electrode extraction current is amenable to one-dimensionalisation, so is the whole system.

## III. APPLICATION TO SCANNING PHOTOCURRENT MICROSCOPY

In scanning photocurrent microscopy, we scan a narrowly focused laser beam over the sample, as illustrated in Figure 5a. We may either scan between electrodes, on top of one electrode, or beyond the active area, next to sets of electrodes. In the first and last case, the electrodes need not only contact the back. We now apply the analysis above to reduce the dimensionality this problem. Under uniform illumination, an infinite back-contact solar cell usually has reflective symmetry about the center of each electrode, however this is broken by localised illumination, necessitating more complex models. The illumination itself has rotational symmetry, but the electrodes occur in laterally symmetric strips; the combination gives us only one line of reflective symmetry through the centre of the illumination.

Experiments usually involve illuminating a film either away from the electrodes (case one, as in [15, 20]), or are on top of one extended electrode (case two, as in [14, 23]) in which case

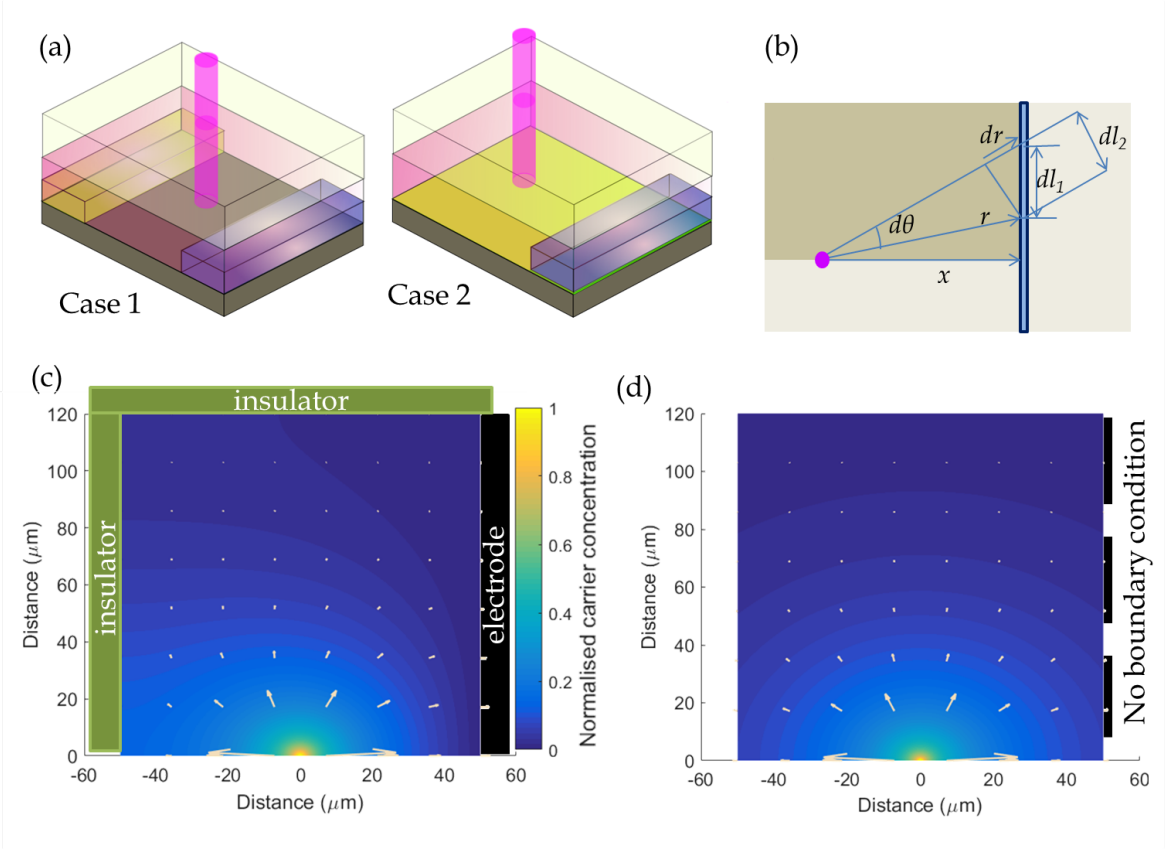


Figure 5. (a): Diagram of point-illumination of back-contact system with two electrodes. In case one, illumination is between electrodes. In case two, one electrode is extended over the whole surface. (b): Top-down view of (a), with one electrode neglected and lengths labelled. Simulated area is shaded darker brown. (c): Numerical solution to the point-excitation problem in 2 dimensions. The solution has a 0-concentration condition imposed at $x = 70$ and zero-flux, reflective boundary conditions at other borders. Excitation is at the origin, where concentration is normalised to one. Arrows indicate current flow. (d): Analytical, Bessel function solution to the point-excitation problem in two dimensions, with no boundary conditions imposed at any border. Note that it matches the y = 0 reflective boundary by symmetry. Excitation is at the origin. Integration to find current performed along the dotted line, representing the electrode. Scale is as in (c), values are normalised to one at half a micron away from the origin and saturated within. (c, d): White arrows indicate direction and magnitude of carrier diffusion.

we will soon extract all of one carrier type and measure only the spread and surface recombination of the remaining carrier. The two cases are illustrated in Figure 5a. In both case one and two, we will see that the general coupled drift-diffusion equations can be simplified into one equation in two dimensions. We begin with the standard three-dimensional steady state drift-diffusion equations:

$$-\nabla \cdot \begin{pmatrix} D_n \nabla n + \mu_n n \mathbf{E} \\ D_p \nabla p - \mu_p p \mathbf{E} \\ -\epsilon \mathbf{E} \end{pmatrix} = \begin{pmatrix} G - R \\ G - R \\ q(p - n) \end{pmatrix}, \quad (4)$$

[24] where $D_{n\,(p)}$ are the electron (hole) diffusion constants, $\mathbf{E}$ is the electric field, $G$ is the generation function and $R$ is recombination. By applying the findings from earlier in the paper, we may two-dimensionalise these three-dimensional equations. The vertical boundary conditions may be replaced by an extraction term subtracted from the right hand side of the first two lines, representing either the effects of electrodes or surface recombination.

In the second case, illuminating over an extended electrode, we have only one carrier in most of the film and may neglect the other.

There may be some recombination before all of one carrier is extracted, meaning that the effective generation function for the remaining carriers is smaller than the actual generation function, however there are no other effects at distances larger than both the beam width and film thickness. In this case we can approximate the carrier generation function to a point source with modified magnitude. We find that the image charge from the electrode cancels out the in-plane space-charge effects of the remaining carrier. The perpendicular electric field may influence the effective extraction velocity but does not influence the horizontal behaviour of the system, therefore for our case of no perpendicular electric field, we can neglect the effects of charge in two dimensions.

This also means that we also need only keep track of one carrier type. As established previously, in most cases we may approximate extraction of carriers from the bottom electrode (or surface recombination there, which appears identical) by an effective bulk extraction, and if recombination is monomolecular, away from the generation region we have the following steady-state equation:

$$D\nabla^2 n - vn = 0 \tag{5}$$

for $D$ the remaining carrier diffusion constant and $v$ the effective surface extraction (or surface recombination) velocity divided by the film height.

A similar situation arises if we have strong enough doping and weak enough illumination that the optically generated carriers are much rarer than the majority dopants, such as in the scanning photocurrent experiments on a transistor performed by Ubrig et al. [19]. Here, the concentration of the majority carrier is largely unchanged by illumination, and only the minority carriers need be tracked.

If we return to case one, a film with no electrode underneath, we may derive a similar equation. In systems like this, both electrons and holes are mobile but have different diffusion constants. Here, we must consider the phenomenon of ambipolar diffusion, where the electrons and holes diffuse together, which occurs when there is no selective extraction or injection of one carrier [25, 26]. The electrostatic attraction between the electrons and holes ensures that the faster species is pulled back and the slower is pulled forwards. This attractive effect will force the distributions of the carriers to be (almost) identical, with a diffusion constant somewhere in between that of electrons and holes. Since their populations behave the same, in our undoped case, $n = p$, the electric fields are screened and there is no long-range net electric field generated by the charges [26]. This means that the last line of equation (4) is not needed, and the first two lines are identical.

The value of the ambipolar diffusion constant is (from [25])

$$D_a = \frac{2D_n D_p(n+p)}{D_n n + D_p p}, \tag{6}$$

however if excitation levels are higher than doping levels (as might be expected for perovskites) then ambipolarity means $n = p$ and so $D_a = 2D_nD_n/(D_n + D_p)$. Assuming we have only monomolecular recombination, which may include both a bulk and an interface component, we can make this the $v$ term in equation (5). The overall behaviour in these two cases can be modelled in the same way.

If our situation is circularly symmetric, equation 5 becomes

$$\frac{D}{r}\partial_r\left(r\partial_r n\right) - vn = 0 \tag{7}$$

$$\Rightarrow\ r^2\partial_r^2 n + r\partial_r n - \frac{v}{D}r^2 n = 0 \tag{8}$$

If we define the inverse of the diffusion length as $a \equiv \sqrt{v/D}$, then we recognise this equation as the zeroth-order modified Bessel's equation with solution

$$n(r) = AK_0\left(ar\right) + BI_0\left(ar\right), \tag{9}$$

an arbitrary sum of the zeroth-order $I$ and $K$ modified Bessel functions. No $I_0$ term is allowed on an infinite plane since it will diverge at large distances. The divergence of $K_0$ at 0 is permissible since we assumed a point generation function, an approximation that is only valid outside the real generation width. A mathematical complication emerges because charges are usually collected by a linear electrode, so we need to integrate this $n$ along a line to compare this fit to measured currents. Also, the electrode absorbs carriers, and may therefore perturb the carrier density, breaking the circular symmetry of the solution. There are two ways to approximate this interaction: either the electrode extraction rate is fast and no carriers are present for $x > x_0$, or it is slow and does not significantly perturb the carrier level. If the extraction is fast, we should impose a boundary condition which breaks the

cylindrical symmetry of the Bessel function solution, whereas we can ignore it for slow extraction.

However by comparing the normalised Bessel function solution with the numerical solution (as seen individually in Figures 5c and d, and compared numerically in Figure 6a), we observe that the 0 carrier condition makes little difference to the solution except close to the electrode and therefore the numerical value of $J(r)$ in the bulk can be estimated accurately from the analytical solution. The symmetry plane at the $x$-axis corresponds to a true 0-derivative (Neumann) boundary condition, which the Bessel function solution respects. We impose similar conditions on the numerical model at the arbitrarily placed upper and left limits (labelled as 'insulators' in Figure 5c), however these are far from the excitation and only locally affect results, as seen in Figure 6a. The impact of the $n = 0$ (Dirichlet) boundary condition on the right is also local, and the Bessel function solution is accurate a short distance away. Furthermore, we see in Figure 6b that, in terms of the net current into the electrode, the impact of this difference is negligible. In the case of moderate recombination ($v$=1 $\mu$s$^{-1}$ so $a = 0.026\ \mu\text{m}^{-1}$), the curves are hard to distinguish, with minor differences in the limit of small surface recombination ($v = 0.1\ \mu\text{s}^{-1}$ so $a = 0.082\ \mu\text{m}^{-1}$), such as might arise in a 300 nm high film with a recombination velocity of 3 cm/s).

Due to the similarity of the results from the two solutions and the tractability of the analytic, boundaryless approximation, we will derive analytic expressions for the current in both the fast and slow extraction cases. In the fast extraction case, the total current can be found by simply taking the line integral of the current density along the electrode. In the slow-extraction regime, the current extracted is proportional to the unperturbed carrier density over the electrode. These two models result in different relationships between current and concentration but it will be shown that after being normalised, they produce identical current trends.

In the slow-extraction limit, we are interested in the integral of the carrier distribution over a line, (see geometry labels in Figure 5b) with elemental length $dl_1 = \sqrt{dr^2 + (rd\theta)^2}$. As we are constrained to $r\cos\theta = x$,

$$dl_1 = \sqrt{dr^2 + \left(\frac{xdr}{\sqrt{r^2 - x^2}}\right)^2} = \frac{rdr}{\sqrt{r^2 - x^2}}. \quad (10)$$

We can then calculate the current,

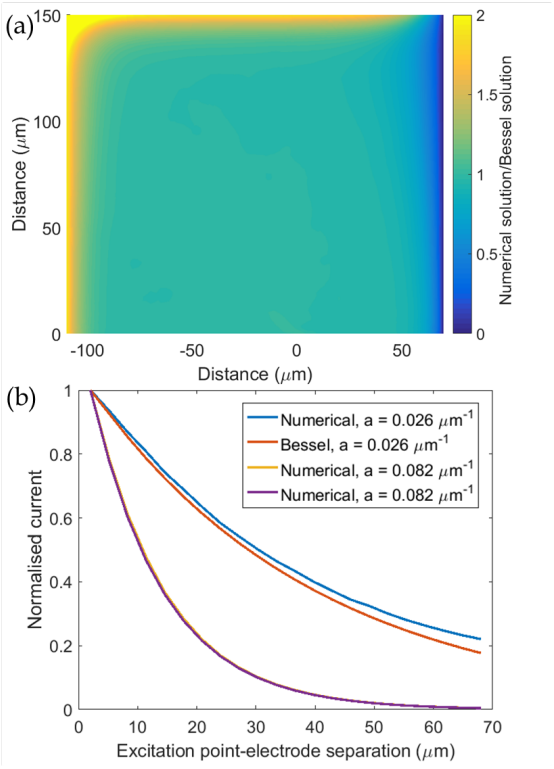


Figure 6. (a): The numerical solution to the point excitation problem divided by the analytic, Bessel function solution. The numerical solution has a 0-concentration condition imposed at $x = 70$ and a zero-flux, reflective boundary conditions at other borders. The analytical solution has no boundary conditions imposed, but matches the y = 0 reflective boundary by symmetry. Excitation is at the origin. (b): Graph of the total currents going into the electrodes in the numerical and Bessel function solutions as the excitation point is moved away from the electrode. Results are for $a$=0.026 $\mu$m$^{-1}$, corresponding to bulk monomolecular recombination in our simulation, or $a = 0.082\ \mu\ \text{m}^{-1}$, corresponding to a very low surface recombination velocity or very tall film (3 cm/s for a 300 nm film). The simulation is conducted in a 100 $\mu$m wide, 120 $\mu$m long box.

$I_1 \propto \int_x^\infty K_0(ar)\frac{rdr}{\sqrt{r^2-x^2}}$. This is integrably singular at $r = x$. Substituting $u = ax$, $y = r/x$, then $w = \sqrt{y^2 - 1}$, we obtain

$$I_1 \propto \int_1^\infty K_0(uy)\, xy \frac{dy}{\sqrt{y^2-1}} \quad (11)$$

$$= x\int_0^\infty K_0\left(u\sqrt{w^2+1}\right) dw. \quad (12)$$

From page 685 of [27] we may compare this with

known integral

$$\int_0^\infty K_\nu\left(m\sqrt{x^2+z^2}\right)\frac{x^{2\mu+1}y}{\sqrt{(x^2+z^2)^\nu}}dx \quad (13)$$

$$=\frac{2^\mu\Gamma(\mu+1)}{m^{\mu+1}z^{\nu-\mu-1}}K_{\nu-\mu-1}(mz). \quad (14)$$

Taking $\nu=0, z=1, \mu=-\frac{1}{2}$, we find

$$I_1\propto\frac{2^{-0.5}\Gamma(0.5)}{u^{0.5}1^{-0.5}}K_{-\frac{1}{2}}(u).$$

Since $\Gamma(0.5)=\sqrt{\pi}$ and $K_{-\frac{1}{2}}(b)=K_{\frac{1}{2}}(b)=\sqrt{\frac{\pi}{2b}}e^{-b}$ (from pages 255 and 444 of [28]),

$$I_1\propto x\frac{\pi e^{-u}}{2u}=\frac{\pi}{2a}e^{-ax}. \quad (15)$$

The end result is we expect to see an exponential decay with length $a^{-1}$, the diffusion length.

Turning to the fast extraction model, we instead use an estimate of the total current from the current contributions we will demonstrate that we obtain the same current decay pattern, in agreement with numerical integration observed by [13]. However this result may also be proven analytically. As shown in Figure 6, the total current as calculated in this way is largely unchanged whether we use the Bessel function solution or the numerical solution. The current is integrated over only the component of the line element orthogonal to the direction of the current, $dl_2=r\,d\theta$, and $J\propto-\frac{dn}{dr}=\frac{-dK_0(ar)}{dr}=aK_1(ar)$, so this estimate of the current $I_2\propto\int_x^\infty K_1(ar)\left(\frac{xdr}{\sqrt{r^2-x^2}}\right)$. Substituting for $t=\left(\frac{r}{x}\right)^2$ and $u=ax$, we obtain

$$I_2\propto\int_1^\infty K_1\left(u\sqrt{t}\right)\left(\frac{dt}{2\sqrt{t}\sqrt{t-1}}\right). \quad (16)$$

This may be compared with the known integral

$$\int_1^\infty K_\nu\left(a\sqrt{x}\right)\frac{dx}{\sqrt{x}\sqrt{x-1}}=\left(K_{\nu/2}\left(\frac{a}{2}\right)\right)^2, \quad (17)$$

from page 683 of [27]. With $\nu=1$, using $K_{\frac{1}{2}}(b)=\sqrt{\frac{\pi}{2b}}e^{-b}$ as above, we find

$$I_2\propto\frac{1}{2}\left(\sqrt{\frac{\pi}{2\alpha}}e^{-\frac{a}{2}}\right)^2=\frac{\pi}{4a}e^{-ax}, \quad (18)$$

and so, comparing with equation (15), we see that we obtain an exponential decay with the same exponent.

The prefactor is different in $I_1$ and $I_2$ (the extraction velocity in the first case and the diffusion constant divided by the diffusion length in the second) however as this is ignored in the normalised result we have a convenient and robust method of analysing the ratio $v/D$, irrespective of the physical origin of $v$. Separating these values may often be accomplished in these models by considering the time delay between excitation and receiving the current.

These results means that in many cylindrically excited situations, we can establish the effective one-dimensional extraction velocity and then current behaviour can be determined analytically. In combination with the findings in the first section, it may be possible to model this extraction using entirely analytical expressions with a high degree of accuracy. Another practical result of this is that, when interpreting current measurements from scanning photocurrent spectroscopy on thin films, we expect the current decay to be monoexponential outside a small radius where generation or second order recombination terms are relevant, and for this result to be independent of the extraction velocity of the electrodes. Interestingly, this solution is identical to the solution of the one-dimensional boundary-free reading of equation (5):

$$D\frac{d^2n}{dx^2}-vn=0 \quad (19)$$

$$\Rightarrow\quad n(x)\propto\exp(-ax) \quad (20)$$

$$\Rightarrow\quad I_{1D}=qD\frac{dn}{dx}\propto\exp(-ax). \quad (21)$$

## IV. TIME-DEPENDENCE OF CURRENT ONSET

The above provides us with a solid way of establishing a combined measurement of $D$ and $v$, but does not disentangle them. However as well as the equilibrium current measurement, scanning current microscopy can investigate the time delay between excitation and current onset, which provides more information about the system. In order to understand how to interpret this delay, we will explore the time-dependent counterpart of equation 5.

In the non-steady state case, following the same assumptions, the carrier concentration is governed by the equation

$$\frac{\partial n}{\partial t}=G-R+D\nabla^2n\ . \quad (22)$$

We note that without the generation ($G$) or recombination/carrier extraction ($R$) terms and ignoring boundary conditions, this is the diffusion equation in 2D [29], with solution

$$n_0(r,t) = A/(4\pi Dt)\,\exp(-r^2/(4Dt))\,.$$

This describes a decaying pattern propagating to reach a position $r$ with characteristic timescale $\tau = r^2/4D$. We can then introduce the $R = vn$ term and can write the new solution as proportional to the old, so that $n = n_0(r,t)\chi_R(t)$

$$\Rightarrow \frac{\partial n_0\chi_R}{\partial t} = -vn_0\chi_R + \chi_R D_n\nabla^2 n_0 \qquad (23)$$

$$= n_0\frac{\partial \chi_R}{\partial t} + \chi_R\frac{\partial n_0}{\partial t}. \qquad (24)$$

We cancel the last terms on the end of each line, from the definition of $n_0$ and so find that $\chi_R(r) \propto \exp(-vt)$. This is then the effective Green's function for the source term, $G$, so if $G = G_0\delta(r)$ after being turned on at time 0 then

$$n = \int_0^t dt' \frac{G_0}{4\pi Dt'}\exp\left(\frac{-r^2}{4Dt'} - vt'\right). \qquad (25)$$

We note that the linearity of this model means that in a steady state, the effects of reducing $G$ will have the same time-dependence as increasing it. This means that if we continuously excite the system, then stop exciting it, the equilibration time for the excitation onset and cessation are identical. However there are two problems with implementing the solution via integration this way: firstly, the integral in 25 is not analytically solvable nor well-behaved numerically; secondly it does not take account of boundary conditions. So, while this can give us some insight into the initial behaviour of the problem, a more useful expression may be obtained by numerical calculation. The solution of equation 22 is computed in MATLAB, with a zero-concentration boundary condition imposed at $x = 0$ and zero derivative boundary conditions at all other boundaries ($x = -100$ $\mu$m, $y = 0$ or 100 $\mu$m). The current density going into the electrode is integrated over the electrode, as in the fast extraction case above. Figure 7a shows the time taken for the current to reach 50% of the equilibrium value as a function of distance from the source, and is roughly linear. We also plot the time taken for currents to reach a small value, corresponding to extracting 2% of the charges excited per unit time. We see that the time for the measured current to reach this value is approximately quadratic, as expected for a diffusing travelling wave to reach a particular position. However, at this time the current itself is rather low, so these values are difficult to measure. The larger fractions, such as the 50% as plotted, is easier to measure but still will suffer from noise in the data. The measure of time most easily and accurately experimentally accessible is the mean time lag that will be detected by a lock-in amplifier, $t_{eq}$.

We assume that the optical excitation is chopped with a square-wave form. The lock-in amplifier takes a signal proportional to the resulting measured current, modulates it with a function at the chopping frequency and time-averages the response by passing it through a low-pass filter. By also calculating the results with a delayed modulating signal, we obtain both the absolute magnitude of the signal response (as used above), and also a phase delay [30]. This phase delay corresponds to a characteristic equilibration time, $t_{eq}$. The precise nature of this relation will depend on the modulating function, as discussed in the supplementary materials. Provided the modulation period $2T_P$ is far longer than any characteristic equilibration time, then for any arbitrary time $T$ such that $T_P \gg T \gg t_{eq}$, the value of $t_{eq}$ can be calculated, where we define

$$t_{eq}(x) = T - \frac{\int_0^T I(x,t)dt}{I(x,T)}, \qquad (26)$$

for $I$ the total current measured at the electrode (we will use the value of $I_2$ to calculate this numerically). A derivation of this relation and how it can be calculated from the phase delay is given in the supplementary materials.

If the boundary conditions are irrelevant, given the linearity of the problem in $G$, there are only two relevant constants, $D$ and $v$. This means we can nondimensionalise $(x,t)$ to $(r\sqrt{v/D}, vt)$. The boundary conditions are still imposed in terms of absolute distance rather than nondimensionalised distance but the effects of this should be minor when the excitation is away from them. We therefore expect to see the dimensionless equilibration time to be a function $vt_{eq} = g(x\sqrt{v/D})$. Figure 7 shows that plotting $t_{eq}$, as calculated from the numerical solutions, against $x$ gives a linear relationship, suggesting $t_{eq} = A(x\sqrt{1/Dv}) + B$ for some $A$ and $B$. To establish what these are, $t_{eq}(x)$ is calculated for a variety of $D$ and $v$ and the relationship is plotted in figure 7b. We find that the end result is

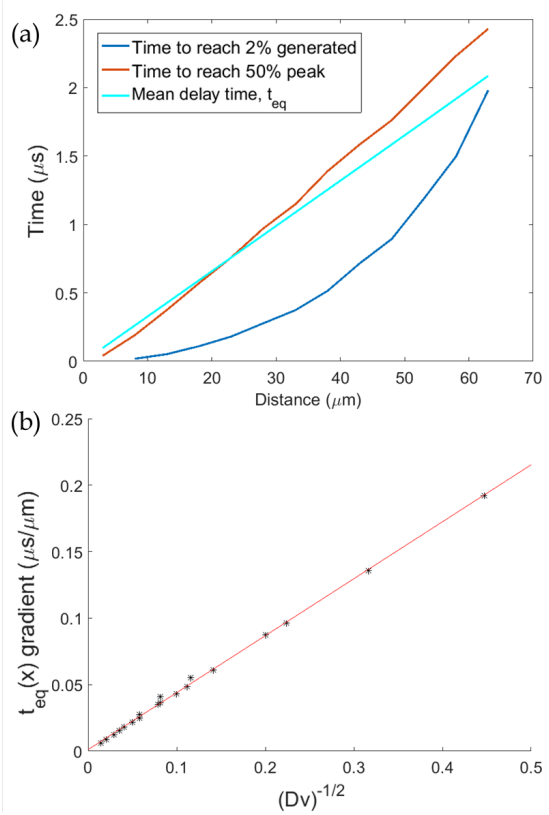


Figure 7. (a): Comparison of the time taken for the current output to reach 50% of the final value, a fixed value equal to 0.2% of the total rate of carrier generation, or $t_{eq}$, as a function of the distance between excitation point and electrode in the single-variable simulation. Data is from a simulation with $D = 1.5$ cm$^2$/s, $v = 1$ $\mu$s$^{-1}$ (b): The spatial gradient of the equilibration time, $dt_{eq}/dx$, is plotted as a function of $1\sqrt{Dv}$ for a variety of $D$ and $v$. As shown in (a), the gradient of $t_{eq}$ is constant for a given set of parameters.

well-fitted by a linear relationship with gradient $0.428 \pm 0.013$.

Conveniently, only the intercept of the linear fit is affected by the common offset errors in $x$ (due to misaligning with the electrode edge) or $t_{eq}$ (from lag in the measurement apparatus) and the intercept is not needed to extract performance metrics. The gradient of the distance-time plot is expected to be $0.43/\sqrt{Dv}$. Between this and the exponential current-time decay proportional to $\sqrt{v/D}$, it is easy to determine both $D$ and $v$ separately.

## V. CONCLUSIONS

In situations featuring large degrees of lateral diffusion, reduced-dimensional modelling or simple analytical expressions will suffice to describe the behaviour of back-contact solar cells or optically excited thin films with laterally displaced electrodes if certain conditions are met. The main conditions are that the system length is long compared to the system width and that fewer than half of the generated charges recombine. In this case it is usually appropriate to neglect the vertical distribution, with an extraction term replacing the vertical surface boundary conditions. If the electrodes extract carriers slowly, this extraction velocity divided by the height is the extraction term. In the fast extraction situation, a more complicated expression for the effective extraction velocity is needed, and it is invalid for very large systems with unequal diffusion constants. Calculating monomolecular recombination levels from one-dimensional and two-dimensional carrier concentrations produces almost identical results in the situations studied here.

This dimension reduction treatment may be implemented on lateral problems exhibiting either one degree of translational symmetry, or on a mixed translational-rotational symmetry problem such as the point illumination of a system with an extended electrode. In the later case, several different commonly-encountered photocurrent microscopy measurements will result in the current recorded exponentially decaying with distance. The exponent factor is the square root of an extraction or recombination rate divided by a diffusion constant, $\sqrt{v/D}$. The time taken for this equilibrium current to be reached will increase linearly with distance, with the gradient being $0.43/\sqrt{Dv}$. Between these two measurements, $v$ and $D$ can therefore be extracted. In photocurrent microscopy measurements, the current equilibrium time can be calculated from the phase delay with a lock-in amplifier. Depending on the placement of the electrodes, the diffusion constant may be that of the electrons, that of the holes, or one in between. If the excitation takes place over one selective electrode, the diffusion constant and extraction rate correspond to the carrier type not extracted. If the excitation takes place in a bulk film, the diffusion constant corresponds to the ambipolar diffusion, a combination of the two diffusion con-

stants, and the decay rate is the recombination rate.

## SUPPLEMENTARY MATERIALS

The supplementary materials has full details of the drift-diffusion simulation setup and parameters. It also details the impact of removing electric field effects, a discussion of how we should consider the errors in the models, the effects of changing both diffusion constants, and the relationship between a lock-in amplifier's phase delay and the equilibration time as defined above.

## ACKNOWLEDGEMENTS

This work was supported by the UK government through the EPSRC. The data underlying this publication are available at [url to be added in proof].

[1] E. Van Kerschaver and G. Beaucarne, Progress in Photovoltaics: Research and Applications **14**, 107 (2006).
[2] N. Zin, A. Blakers, K. R. McIntosh, E. Franklin, T. Kho, K. Chern, J. Wong, T. Mueller, A. G. Aberle, Y. Yang, X. Zhang, Z. Feng, Q. Huang, and P. J. Verlinden, Energy Procedia **33**, 50 (2013).
[3] C. M. Hangarter, B. H. Hamadani, J. E. Guyer, H. Xu, R. Need, and D. Josell, Journal of Applied Physics **109** (2011), 10.1063/1.3561487.
[4] E. Moulin, T. C. M. Müller, M. Warzechac, A. Hoffmann, U. W. Paetzold, and U. Aeberhard, EPJ Photovoltaics **6**, 60501 (2015).
[5] J. Geissbuhler, S. D. Wolf, A. Faes, N. Badel, Q. Jeangros, A. Tomasi, L. Barraud, A. Descoeudres, M. Despeisse, and C. Ballif, IEEE Journal of Photovoltaics **4**, 1055 (2014).
[6] A. Jungel, *Transport Equations for Semiconductors*, Lecture Notes in Physics, Vol. 773 (Springer Berlin Heidelberg, Berlin, Heidelberg, 2009).
[7] J. A. Carrillo, I. M. Gamba, A. Majorana, and C.-W. Shu, Journal of Computational Electronics **2**, 375 (2003).
[8] M. Fournié, Applied Numerical Mathematics **33**, 381 (2000).
[9] G.-L. Tan, X.-L. Yuan, Q.-M. Zhang, W. Ku, and A.-J. Shey, IEEE Transactions on Computer-Aided Design of Integrated Circuits and Systems **8**, 468 (1989).
[10] F. Brezzi, L. D. Marini, and P. Pietra, SIAM Journal on Numerical Analysis **26**, 1342 (1989).
[11] A. Mauri, A. Bortolossi, G. Novielli, and R. Sacco, Journal of Mathematics in Industry **5**, 1 (2015).
[12] NREL, "Best research-cell efficiencies," (2017).
[13] R. Graham and D. Yu, Modern Physics Letters B **27**, 1330018 (2013).
[14] S. Mukhopadhyay, A. J. Das, and K. S. Narayan, The Journal of Physical Chemistry Letters **4**, 161 (2013).
[15] L. M. Pazos-Outon, M. Szumilo, R. Lamboll, J. M. Richter, M. Crespo-Quesada, M. Abdi-Jalebi, H. J. Beeson, M. Vrucinic, M. Alsari, H. J. Snaith, B. Ehrler, R. H. Friend, and F. Deschler, Science **351**, 1430 (2016).
[16] D. Kabra and K. Narayan, Advanced Materials **19**, 1465 (2007).
[17] B. A. Ruzicka, L. K. Werake, H. Samassekou, and H. Zhao, Applied Physics Letters **97**, 262119 (2010).
[18] S. Mukhopadhyay and K. S. Narayan, Applied Physics Letters **100**, 163302 (2012).
[19] N. Ubrig, S. Jo, H. Berger, A. F. Morpurgo, and A. B. Kuzmenko, Applied Physics Letters **104**, 171112 (2014), arXiv:1404.7691v1.
[20] C. J. Lombardo, M. S. Glaz, Z.-E. Ooi, D. A. Vanden Bout, and A. Dodabalapur, Physical Chemistry Chemical Physics **14**, 13199 (2012).
[21] E. Edri, S. Kirmayer, S. Mukhopadhyay, K. Gartsman, G. Hodes, and D. Cahen, Nature Communications **5**, 3461 (2014).
[22] A. Jumabekov, E. Della Gaspera, Z.-q. Xu, A. Chesman, J. van Embden, S. Bonke, Q. Bao, D. Vak, and U. Bach, Journal of Materials Chemistry C **4**, 3125 (2016).
[23] D. Kabra, S. Shriram, N. S. Vidhyadhiraja, and K. S. Narayan, Journal of Applied Physics **101**, 064510 (2007).
[24] S. Bandyopadhyay, *Physics of Nanostructured Solid State Devices* (Springer, 2012) p. 551.
[25] D. A. Neamen, *Semiconductor physics and devices: basic principles*, 3rd ed. (McGraw-Hill, 2003) p. 746.
[26] K. Seeger, *Semiconductor Physics: an Introduction* (Springer-Verlag, 1973) p. 525.
[27] I. S. Gradshtein, R. I. Moiseevich, and A. Jeffrey, *Table of Integrals, Series, and Products* (Academic Press, 2000) p. 1163.
[28] M. Abramowitz and I. A. Stegun, *Handbook of Mathematical Functions with Formulas, Graphs, and Mathematical Tables* (Dover Publications, 1972) p. 1046.

[29] K. F. Riley, M. P. Hobson, and S. J. Bence, *Mathematical Methods For Physics and Engineering* (Cambridge University Press, 2006).

[30] K. G. Libbrecht, E. D. Black, and C. M. Hirata, American Journal of Physics **71**, 1208 (2003).